IEEE Access
Multidisciplinary ⋮ Rapid Review ⋮ Open Access Journal

Received 29 January 2024, accepted 10 February 2024, date of publication 19 February 2024, date of current version 23 February 2024.

Digital Object Identifier 10.1109/ACCESS.2024.3366997

RESEARCH ARTICLE

Implementation of a Bidirectional 400–800V Wireless EV Charging System

SEN-TUNG WU AND YU-WEI CHIU
Innovative Energy Laboratory, Department of Electrical Engineering, National Formosa University, Huwei, Yunlin 632301, Taiwan
Corresponding author: Sen-Tung Wu (stwu@nfu.edu.tw)

ABSTRACT A non-contact isolated bidirectional symmetrical resonant converter with dual active bridge as the main structure is proposed in this study. This scheme is combined with the symmetrical resonant network and integrated into an isolated bidirectional symmetrical resonant conversion circuit. The symmetrical resonance technique is used in this work to realize the voltage regulation of a wide range of output and the function of soft switching under the appropriate operating frequency; reduce the electromagnetic noise and power loss caused by hard switching of power switches in the circuit; and improve the overall converter efficiency, voltage regulation, and hard switching from conventional bidirectional converters. In addition, a pair of non-contact loosely coupled inductors (wireless coils) is used to replace the conventional transformer to transfer the bidirectional energy wirelessly. The digital signal processor TMS320F28335 is the control core of the system in this study. The proposed converter with DC grid input voltage is set to 400 V, and the EV battery side is set to 670–800 V. The rated power capacity of the bidirectional wireless charger is 2 kW. Besides, the proposed bidirectional wireless EV charger has CC-CV charging function to achieve the EV charging requirement. Finally, the maximum efficiency of forward charging mode (grid to vehicle [G2V; 400 V charge to 800 V]) can reach 90.2% while that of reverse discharging mode (vehicle to grid [V2G; 800V discharge to 400V]) can reach 91.4%.

INDEX TERMS Bidirectional resonant converter, symmetric resonant circuit, soft switching, wireless power transfer, loosely coupled inductor.

I. INTRODUCTION

Human requirements for various resources of technologies on the earth have increased for the advancement and improvement of technology, but the impact of the development of science and technology on the environment has also intensified. Accordingly, the development and application of renewable energy are necessary to reduce the dependence on traditional energy and impact on the environment. Among the types of renewable energy, conversion and utilization of natural resources, such as wind, solar energy, and water power, are the most common [1], [2]. However, power generation is very unstable because renewable energy is typically subjected to natural factors, such as weather and season. This problem of instability will lead to insufficient power supply during peak power consumption and excess power generation during off-peak period. Therefore, energy conversion plays an important role in the development between storage, and renewable energy [3]. The overall system demonstrates disadvantages of large size and high cost because it must be composed of multiple sets of converters given that energy storage and release of batteries require a converter device. If a bidirectional converter [4], [5] can be used to replace the traditional structure, then the whole system can stabilize through its bidirectional power transmission structure while improving the efficiency of the whole converter and maximizing the utilization rate of energy. Fig. 1 shows the energy storage and release concept [6] that combines renewable energy and a two-way energy storage system. For energy storage, DC power source is mostly used for energy storage and batteries. Many studies [7], [8], [9] have recently proposed that the DC grid can deliver the energy in the electric vehicle

The associate editor coordinating the review of this manuscript and approving it for publication was Valerio De Santis.

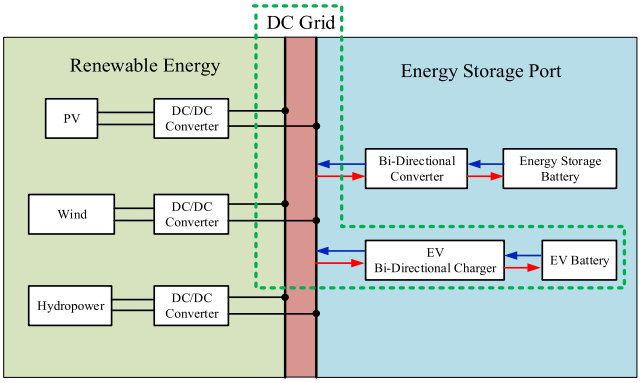

FIGURE 1. Concept of V2G and G2V.

battery (G2V), and the electric vehicle battery can release energy to the DC grid (V2G). The concept of two-way charging and discharging for the electric vehicle with discharging function can recharge the vehicle energy back to the grid when a demand exists for electricity in the grid, thereby converting into a virtual power plant (Note: PV➜Photovoltaic). In this paper, the green-dotted block is the main structure of the study. The post-stage of PV, wind, hydro power is connected to a DC/DC converter to boost the output DC level to 400 V to DC grid. After that, the EV Bi-directional charger can charge EV battery to 800 V. In nowadays, EV battery voltage increases to 800 V for several advantages [10].

The first one is the charging time for 800V EV battery is almost half of 400V EV battery under the same charging power level. The second one is that the charging current for 800V EV battery is half lower than 400V EV battery. It means that the diameter of the charging cable can be smaller if charging in 800V EV battery scenario. In other words, the wire of an 800V EV can save more cost with smaller charging current.

The LLC is a common topology for resonant converters [11], [12], [13]. The ability of the LLC resonant converter to realize zero-voltage switching under a wide range of loads and zero-current switching in a specific resonance region can sufficiently improve the efficiency of the converter. However, LLC resonant converters still present some drawbacks. When applied the converter bidirectionally, the maximum voltage gain of 1 operated in reverse mode complicates the bidirectional power conversion as well as the design.

The wireless power transfer (WPT) system with transmitting and receiving coils mainly designed for industrial applications requires high switching frequency to achieve a sufficiently high power density [14]. The circuit architecture similar to an LLC converter can simplify the receiving circuit; hence, the compensation capacitor on the secondary side can be omitted. The experimental results showed a peak efficiency of 92% at 2 MHz.

In addition, a bidirectional wireless EV charging system from [15] provides a zero-phase-angle controlled technique which gives a simple control strategy for a bidirectional wireless EV charging system to keep the rated power level with the maximum efficiency when the transmitting and receiving coils are misalignment. The basic topology of this bidirectional converter operated for 1 kW is based on series-series compensation network. However, the input voltage and the output voltage are identical for 200Vdc, the equivalent input/output voltage helps to simplify the coils design with the same turns ratio. According to [16] the proposed bidirectional wireless EV charging system which the primary and secondary converters are both being controlled actively. The phase synchronization technique between the two converters are required to control the power flow direction. This study gave a new phase synchronization method by tracking the maximum of the output current, without auxiliary hardware or the real- time communication between the primary and secondary sides. The control technique is novel; however, the power loss on MOSFET caused by hard switching of the proposed scheme is a challenge.

At present, electric vehicle charging methods [17], [18] can be divided into four types, namely, conventional cable charging, fast cable charging, battery exchange, and wireless charging technique for energy transfer. Magnetic induction (MI) and magnetic resonance (MR) are two common wireless charging mechanisms. The mature magnetic induction technique presents excellent transmission efficiency at short transmission distances. On the basis of these research motivations, a bidirectional converter with the theme of electric vehicles [19] is developed in this study using a conventional LLC resonant converter to achieve soft switching characteristics [20] in the full range of both directions. The results showed that zero-voltage and zero-current switching can improve the overall efficiency of the converter. In [21], it focuses on the development of a bidirectional wireless charging system for EV. The bidirectional DC-DC converter utilizes a separately designed LCC resonant tank for both sides of the source and the vehicle. Employing bidirectional power switches, the converters function as inverters or rectifiers depending on the power flow direction. The DC link voltage on the grid side is configured to be in the range of 700-800V for three phases, whereas the battery side operates at a DC link voltage of 350-400V to optimize power transfer efficiency. The designed converter is capable of handling a power capacity of 10KW. However, the switching frequency is 25kHz which is lower switching frequency, while reducing switching losses, result in larger volumes for magnetic components and also impose limitations on the voltage regulation range. In [22], the hybrid modulation strategy for the LCC–LCC compensation in a bidirectional wireless power transfer system (LCC-BWPT) was proposed with the aim of enhancing efficiency across the entire operational range. The fundamental operating modes of LCC-BWPT with the hybrid modulation strategy were analyzed, and a unified discrete-time model was established based on full-mode operation, accurately describing the state variables under all operating modes. Using this model, optimal operation criteria were proposed, considering the three operational processes of LCC-BWPT: constant current (CC) charging process,

constant voltage charging process, and CC discharging process. Optimal control variables for each of the three processes were derived, achieving zero-voltage switching operation and minimizing reactive power flow. In [23], this research presents the design and demonstration of a bidirectional 20 kW wireless charging system (WCS) with a significantly large air gap and asymmetric input-output voltage levels. The resonance circuit of the WCS was analyzed, and sensitivity analysis experiments were conducted to verify the optimal operating region under load and frequency variations. The inverter and rectifier employ switch component designs, the charging pad adopts a dual-D (DD) coil design, and the regulating network is designed with an LCC-LCC modulation circuit. Regulating circuits for both the grid and vehicle sides were separately designed to achieve approximately a 1:2 gain for asymmetric input (800 Vdc) and output (350 Vdc) voltages.

In comparison with the outcomes and the characteristics of LLC and LCC resonant structures [24], it is observed that the LLC resonant structure is well-suited for operation in a low-voltage and high-current working mode, whereas the LCC resonant structure is suitable for operation in a high-voltage and low-current working mode. Both LLC and LCC resonant topologies can be used for wireless charging circuit which depend on the applications of the voltage and current demands.

In order to meet the specifications and requirements of this research, LLC compensation network is chosen as the main bidirectional converter scheme. The symmetrical resonant technique and pulse frequency modulation to achieve output voltage regulation. The soft-switching functionality is attainable at suitable operating frequencies for reducing electromagnetic noise and power losses caused by hard switching of circuit power switches. This approach enhances the overall converter efficiency and stability, addressing issues related to voltage regulation and hard switching in the proposed wireless bidirectional converters. Besides, the topology of LLC and LCC are almost the same but different resonant gain curve shapes and different resonant components [24]. LLC resonant structure is mainly used in low-voltage applications while LCC resonant structure is in high-voltage applications.

II. ANALYSIS OF THE PROPOSED CONVERTER

A. PROPOSE CONVERTER CONFIGURATION

An isolated bidirectional symmetrical resonant converter is proposed and implemented in this study. The circuit structure is shown in Fig.2. The forward charging mode is defined as the grid port that supplies power to the battery energy storage and discharge port. Meanwhile, the reverse discharge mode is defined as the battery port that supplies power to the grid port. The characteristics of this circuit are similar to those of a bidirectional LLC resonant converter [25]. A resonant element is added on the load side, and rectifier diodes on the secondary side of the traditional LLC resonant circuit transformer are replaced by rectifier switches. The function of two-way energy transfer.

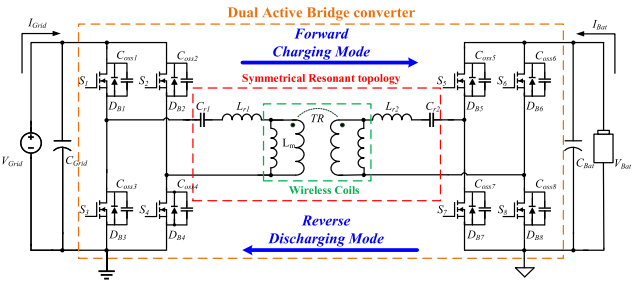

FIGURE 2. Proposed isolated bidirectional symmetrical resonant converter circuit.

The voltage gain curve based on design parameters of the bidirectional resonant converter obtained through the mathematical operation simulation software Mathcad is illustrated in Fig. 3 The gain curve in the forward charging mode operation shows that the full-bridge resonant converter adopts a symmetrical resonance parameter design to ensure that the forward and reverse voltage gain curves are similar. Its gain varies with the switching frequency and can be divided into three intervals according to the resonant frequency(f_r).

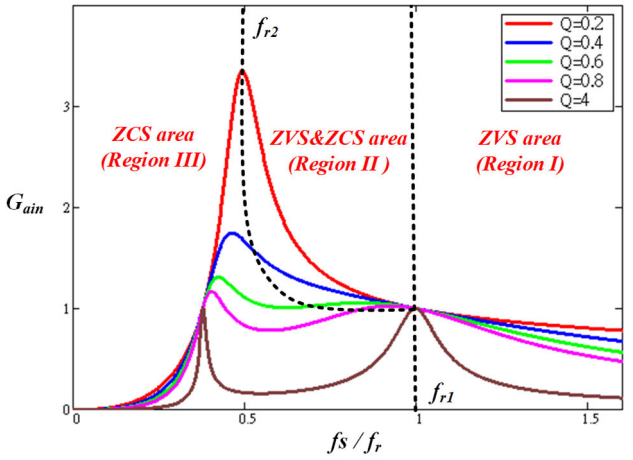

FIGURE 3. Gain characteristic curve of the proposed converter.

The resonant tank of the converter is inductive and the primary side power switches can achieve zero-voltage switching [26] when the circuit operates in Region I. Meanwhile, the resonant tank of the converter is inductive and enables power switching when the circuit operates in Region II. The resonant tank in the circuit enters the decoupling interval when the switches achieve the zero-voltage switching function [27]. The rectifier diode current naturally drops to zero and the secondary side rectifier switch reaches zero because the controlled side fails to transmit energy to the load side during the decoupling interval. The current switching effect achieves the optimal range in design because it can sufficiently reduce power loss and effectively improve the overall conversion efficiency of the circuit. The resonant tank of the converter is controllable and capacitive when the circuit operates in Region III. Failure of the side power switch to achieve

the effect of ZVS results in a large amount of power loss, recharging of the load energy to the controlled side during the operation process, and damage of the switch. Therefore, this type of failure should be avoided when designing the voltage gain and operating frequency.

B. OPERATION PRINCIPLES

The symmetric resonant circuit in this study presents the characteristics of soft switching to ensure that the power switches can achieve zero-voltage switching function in bidirectional circuit operation. When the converter operates in an appropriate resonance range. Meanwhile, the zero-current switching effect of the secondary side rectifier switch can reduce a considerable amount of power loss and effectively improve the overall conversion efficiency of the circuit. Fig. 4 shows the theoretical waveform of the converter operating in Region II, and its operation principle will be introduced in operating stages I to VI. The six modes of the positive half cycle are taken as an example in the analysis given that the operation principle of the negative half cycle is similar to that of the positive half cycle.

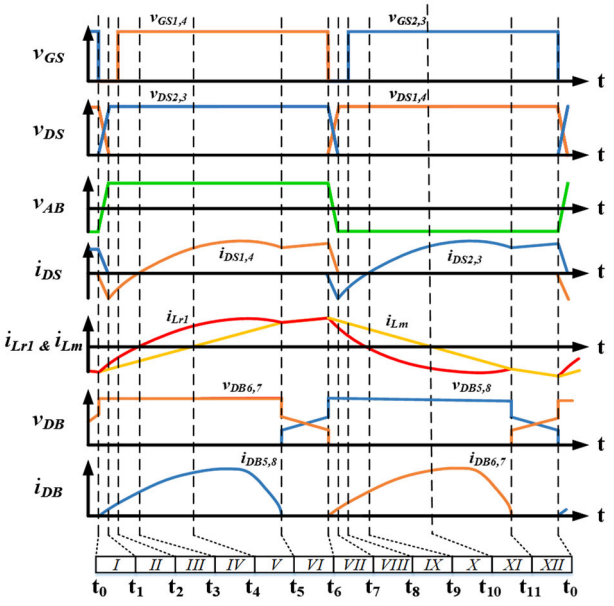

FIGURE 4. Theoretical waveforms related to the main components of the converter operating in Region II.

1) OPERATING STAGE I ($t_0 < t \leq t_1$)

As shown in Fig. 5, gate signals v_{GS2} and v_{GS3} of power switches S_2 and S_3 enter the off state from the on state while power switches S_1 and S_4 remain off and the circuit enters the dead time when $t = t_0$. The resonant current i_{Lr1} maintains the current direction, and parasitic capacitances C_{oss1} and C_{oss4} of the power switch release energy through i_{Lr1} while i_{Lr1} stores energy for C_{oss2} and C_{oss3}. In addition, the current difference transmits energy to the secondary side through the wireless coils and rectifies the output through body diodes D_{B5} and D_{B8} given that i_{r1} and i_{Lm} are not equal.

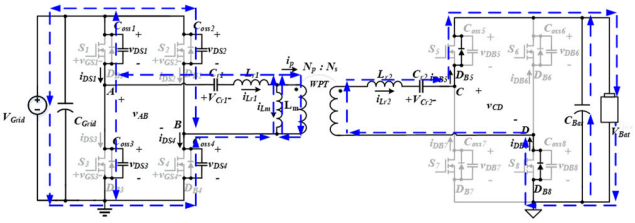

FIGURE 5. The current path in the operating stage I.

This operation stage ends when parasitic capacitances C_{oss1} and C_{oss4} of the power switch are completely discharged to zero and C_{oss2} and C_{oss3} are charged to V_{Grid}.

2) OPERATING STAGE II ($t_1 < t \leq t_2$)

As shown in Fig. 6, power switches S_1 to S_4 are all turned off when $t = t_1$. The resonant current i_{Lr1} forms a freewheeling state through body diodes D_{B1} and D_{B4} of the power switch to ensure that power switches S_1 and S_4 form the zero-voltage switching condition. The function of zero-voltage switching can be realized when S_1 and S_4 are turned on. At this time, i_{Lr1} continues to provide energy to the secondary side to allow diodes D_{B5} and D_{B8} to conduct. Gate signals v_{GS1} and v_{GS4} of power switches S_1 and S_4 go from the off state to the on state and this operating stage ends when $t = t_2$.

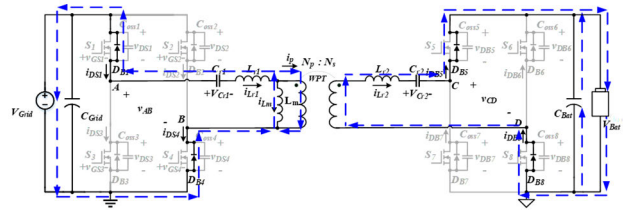

FIGURE 6. The current path in the operating stage II.

3) OPERATING STAGE III ($t_2 < t \leq t_3$)

As shown in Fig. 7, S_1 and S_4 are turned on and the power switches achieve the function of zero-voltage switching when $t = t_2$. At this time, i_{Lr1} and i_{Lm} continue to rise and transmit energy to the secondary side through the wireless coils and rectified by body diodes D_{B5} and D_{B8}. The magnetizing current i_{Lm} continues to rise linearly because the magnetizing inductor L_m is affected by the clamping of the output voltage V_{Bat} and the secondary side resonant capacitor voltage V_{Cr2}

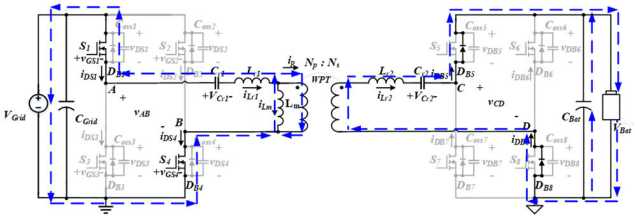

FIGURE 7. The current path in the operating stage III.

to ensure that the magnetizing inductor L_m does not participate in the resonance. This working phase ends when the resonant current $i_{Lr1} = 0$.

4) OPERATING STAGE IV ($t_3 < t \leq t_4$)

As shown in Fig. 8, power switches S_1 and S_4 remain turned on and the resonant current i_{Lr1} changes from negative to 0 when $t = t_3$. At this time, V_{Grid} resonates through C_{r1}, C_{r2}, L_{r1}, and L_{r2} to ensure that the resonant current i_{Lr1} and the magnetizing current i_{Lm} are not equal, and the current difference is transmitted through the wireless coils to transmit energy to the secondary side and then rectified by body diodes D_{B5} and D_{B8} for output. Note that the magnetizing current i_{Lm} continues to rise linearly and the magnetizing inductance L_m does not participate in the resonance because the magnetizing inductor L_m is affected by the clamping of the output voltage V_{Bat} and the secondary side resonant capacitor voltage V_{Cr2}. The slope of i_{Lr1} gradually decreases given that the voltage across C_{r1} is increasing. This operating stage ends when the magnetizing current $i_{Lm} = 0$.

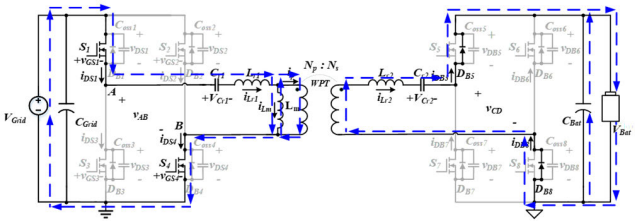

FIGURE 8. The current path in the operating stage IV.

5) OPERATING STAGE V ($t_4 < t \leq t_5$)

As shown in Fig. 9, power switches S_1 and S_4 remain on and the direction of the magnetizing current i_{Lm} changes when $t = t_4$. At this time, the current difference between the resonant i_{Lr1} and magnetizing current i_{Lm} increases and the energy is transmitted to the secondary side through the wireless coils and then rectified by body diodes D_{B5} and D_{B8} for output. The magnetizing current i_{Lm} continues to rise linearly because the magnetizing inductor L_m is affected by the clamping of the output voltage V_{Bat} and the secondary side resonant capacitor voltage V_{Cr2} to ensure that the magnetizing inductor L_m does not participate in the resonance. This operating stage ends when i_{Lr1} is equal to i_{Lm}.

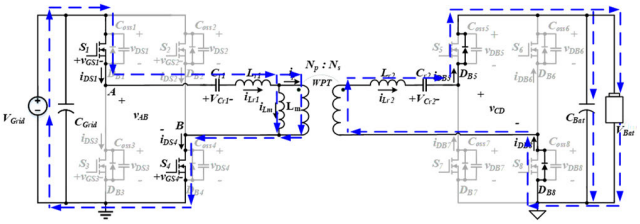

FIGURE 9. The current path in the operating stage V.

6) OPERATING STAGE VI ($t_5 < t \leq t_6$)s

As shown in Fig. 10, power switches S_1 and S_4 remain on and power switches S_2 and S_3 remain off when $t = t_5$. i_{Lr1} and i_{Lm} are equal when $t = t_5$. At this time, the resonant tank enters the decoupling interval and current flow is absent in the secondary which is similar to an open circuit. Therefore, the current in the secondary of the body diode is reduced to zero. Thus, the function of zero-current switching is achieved. The magnetizing inductor L_m is not clamped by the output voltage V_{Bat} and the secondary side resonant capacitor voltage V_{Cr2} given that the wireless coils do not transmit energy to the secondary side. Hence, the resonance in this interval is only achieved by L_{r1}, C_{r1}, and L_m while L_{r2} and C_{r2} do not participate in resonance. This operating stage ends when $t = t_6$ and gate signals v_{GS1} and v_{GS4} of power switches S_1 and S_4 turn from the on state to the off state. The positive half-cycle operating principles end here, and the next operation principle is the negative half-cycle. The operating principle of the negative half cycle will not be described in this work because of its similarity to the positive half cycle.

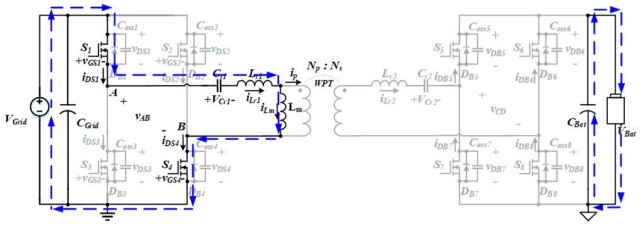

FIGURE 10. The current path in the operating stage VI.

C. ANALYSIS OF VOLTAGE GAIN CHARACTERISTICS

1) DERIVATION OF VOLTAGE GAIN IN FORWARD CHARGING MODE

In order to analyze the resonant circuit, Fundamental Harmonic Approximation (FHA) is widely employed method for analyzing equivalent models. To gain a deeper understanding of the design of bidirectional symmetrical resonant circuits and to derive the relationship between voltage gain and switching frequency, an AC equivalent circuit model based on the FHA analysis method is discussed. As depicted in Fig. 11 this is the AC equivalent model for the forward charging mode. The equivalent model of the loosely coupled inductor is similar to that of a conventional transformer.

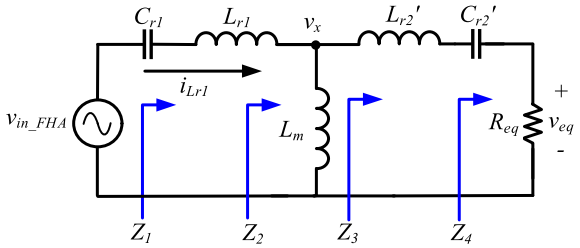

FIGURE 11. AC equivalent circuit for forward charging mode.

The voltage gain characteristic curves shown from Fig. 13 to Fig. 16 are illustrated through the mathematical software, Mathcad, to help in designing the circuit and analyzing its characteristics for forward charging mode. The influence of different resonant parameters vary on the gain curves is analyzed, and its characteristics are described. The following descriptions are all in the forward charging mode. The resonant characteristic curve is illustrated to facilitate the derivation.

v_{in_FHA} represents the fundamental magnitude of square wave voltage generated by the primary-side switches. v_{eq} represents the fundamental magnitude of voltage across R_{eq}. The primary-side resonant capacitor, C_{r1}, the primary-side resonant inductor, L_{r1}, and the magnetizing inductor, L_m are stated clearly. The equivalent resonant capacitor, C'_{r2}, and the equivalent resonant inductor, L'_{r2}. Both of them are reflected from the secondary side. The equivalent load R_{eq} is reflected from the battery terminal to the primary-side. Expression of R_{eq} is shown in equation (1).

$$R_{eq} = \frac{8N^2}{\pi^2} \cdot \frac{V_{bat}}{I_{bat}} = \frac{8N^2}{\pi^2} R_{bat} \tag{1}$$

In this equation, N represents the turns ratio of the loosely coupled inductor, and R_{bat} is the equivalent impedance of the battery load (V_{bat}/I_{bat}). In order to derive the gain relationship between the output and input of the AC equivalent circuit, a node voltage, v_x is set for voltage division relationship of the input and output with respect to v_x. which are shown in equation (2) to (3) with s-domain formation.

$$v_x(s) = v_{\text{in\_FHA}}(s) \cdot \frac{Z_2(s)}{Z_1(s)} \tag{2}$$

$$v_{eq}(s) = v_x(s) \cdot \frac{Z_4(s)}{Z_3(s)} \tag{3}$$

where $Z_1(s)$, $Z_2(s)$, $Z_3(s)$, and $Z_4(s)$ represent the equivalent impedances from the Z_1, Z_2, Z_3, and Z_4 terminals to the output side which are shown in equation (4) to (7).

$$Z_1(s) = sL_{r1} + \frac{1}{sC_{r1}} + Z_2(s) \tag{4}$$

$$Z_2(s) = \frac{sL_m \cdot (sL_{r2}' + \frac{1}{sC_{r2}'} + R_{eq})}{sL_m + sL_{r2}' + \frac{1}{sC_{r2}'} + R_{eq}} \tag{5}$$

$$Z_3(s) = sL_{r2}' + \frac{1}{sC_{r2}'} + R_{eq} \tag{6}$$

$$Z_4(s) = R_{eq} \tag{7}$$

By combining equations (4) to (7), the forward gain $M_{vr\_forward}$ can be derived from the AC equivalent circuit when the converter operates in the forward charging mode. This relationship is expressed in equation (8).

$$\begin{aligned} M_{vr\_forward}(s) &= \frac{v_{eq}(s)}{v_{in\_FHA}(s)} = \frac{v_x(s)}{v_{in\_FHA}(s)} \cdot \frac{v_{eq}(s)}{v_x(s)} \\ &= \frac{Z_2(s)}{Z_1(s)} \cdot \frac{Z_4(s)}{Z_3(s)} \\ &= \frac{sL_m // (sL_{r2}' + \frac{1}{sC_{r2}'} + R_{eq})}{sL_{r1} + \frac{1}{sC_{r1}} + [sL_m // (sL_{r2}' + \frac{1}{sC_{r2}'} + R_{eq})]} \\ &\quad \cdot \frac{R_{eq}}{sL_{r2}' + \frac{1}{sC_{r2}'} + R_{eq}} \end{aligned} \tag{8}$$

L_{r2}' and C_{r2}' are reflected from the secondary-side; therefore, the turns ratio, N needs to be considered. They are defined as follows:

$$L_{r2}' = N^2 L_{r2} \tag{9}$$

$$C_{r2}' = \frac{1}{N^2} C_{r2} \tag{10}$$

In order to simplify the mathematical expressions of the characteristics gain curves, the definition the parameters are summarized in Table1.

TABLE 1. Parameter definition for forward charging mode.

Parameters	Definition
$m_1 = \frac{L_{r2}'}{L_{r1}}$	Resonant inductor ratio
$g_1 = \frac{C_{r2}'}{C_{r1}}$	Resonant capacitor ratio
$k_1 = \frac{L_m}{L_{r1}}$	Ratio of magnetizing inductor and resonant inductor
$q_1 = \frac{\sqrt{\frac{L_{r1}}{C_{r1}}}}{R_{eq}}$	Quality factor
$f_{r1\_f} = \frac{1}{2\pi\sqrt{L_{r1}C_{r1}}}$	First resonant frequency
$f_{n1\_f} = \frac{f_s}{f_{r1\_f}}$	The ratio of switching frequency to the first resonant frequency

By substituting the parameters in Table 1 into equation (8), the voltage gain in forward charging mode is simplified in equation (11), as shown at the bottom of the next page. This equation shows the relationship between resonant components, quality factor, resonant frequency, and switching frequency.

2) DERIVATION OF VOLTAGE GAIN IN REVERSE DISCHARGING MODE

The circuit architecture is a symmetrical resonant network. Hence, the analysis methods and steps for the reverse discharging mode are the same as the forward charging mode, the AC equivalent model is shown in Fig. 12 V_{bat_FHA} represents the fundamental magnitude of square wave voltage generated by the secondary-side switches. $V_{eq'}$ represents the fundamental magnitude of square wave voltage influenced by the resonant components and loosely coupled inductor. The equivalent resonant components on the secondary-side are denoted as C_{r2}, L_{r2}. The resonant components on the primary-side are denoted as C_{r1}', and L_{r1}' respectively.

L_m' is reflected from the magnetizing inductor on the primary-side. The equivalent load $R_{eq'}$ can be expressed in equation (12).

$$R'_{eq} = \frac{\frac{8}{\pi^2} \cdot \frac{V_{Grid}}{I_{Grid}}}{N^2} = \frac{\frac{8}{\pi^2} \cdot R_{Grid}}{N^2} \tag{12}$$

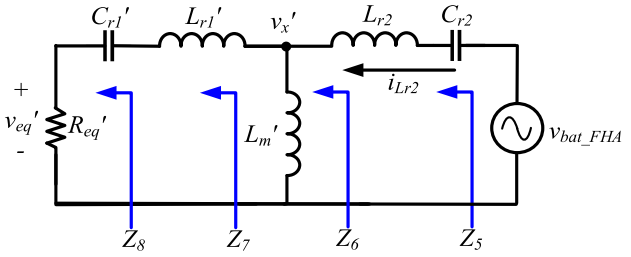

FIGURE 12. AC equivalent circuit for reverse discharging mode.

In equation (12), R_{Grid} (V_{Grid}/I_{Grid}) is the equivalent load of the grid port. In order to obtain the gain relationship between the output and input from the AC equivalent circuit, $v_{x'}$ nodal voltage division is utilized again. By using this voltage division, the relationship between the input and output with respect to $v_{x'}$ is shown in equation (13) to (14).

$$v_x{}'(s) = v_{bat\_FHA}(s) \cdot \frac{Z_6(s)}{Z_5(s)} \tag{13}$$

$$v_{eq}{}'(s) = v_x{}'(s) \cdot \frac{Z_8(s)}{Z_7(s)} \tag{14}$$

$Z_5(s)$, $Z_6(s)$, $Z_7(s)$, and $Z_8(s)$ represent the equivalent impedances Z_5, Z_6, Z_7, and Z_8 terminals to the output side with blue arrows in Fig. 12 The expressions are also shown in equation (15) to (18).

$$Z_5(s) = sL_{r2} + \frac{1}{sC_{r2}} + Z_6(s) \tag{15}$$

$$Z_6(s) = \frac{sL_{m'} \cdot (sL_{r1'} + \frac{1}{sC_{r1'}} + R_{eq'})}{sL_{m'} + sL_{r1'} + \frac{1}{sC_{r1'}} + R_{eq'}} \tag{16}$$

$$Z_7(s) = sL_{r1}{}' + \frac{1}{sC_{r1}{}'} + R_{eq}{}' \tag{17}$$

$$Z_8(s) = R_{eq}{}' \tag{18}$$

By summarizing equations (15) to (18), the derivation of the input/output of the AC equivalent circuit when the converter operates in the reverse discharge mode is expressed in equation (19).

$$\begin{aligned} M_{vr\_reverse}(s) &= \frac{v_{eq}{}'(s)}{v_{bat\_FHA}(s)} = \frac{v_x'(s)}{v_{bat\_FHA}(s)} \cdot \frac{v_{eq}'(s)}{v_x'(s)} \\ &= \frac{Z_6(s)}{Z_5(s)} \cdot \frac{Z_8(s)}{Z_7(s)} \\ &= \frac{sL_{m'}//(sL_{r1'}+\frac{1}{sC_{r1'}} + R_{eq'})}{sL_{r2} + \frac{1}{sC_{r2}} + [sL_{m'}//(sL_{r1'}+\frac{1}{sC_{r1'}} + R_{eq'})]} \\ &\quad \cdot \frac{R_{eq'}}{sL_{r1'}+\frac{1}{sC_{r1'}} + R_{eq'}} \end{aligned} \tag{19}$$

L_{r1}' and $C_{r1}{}'$ are reflected from the primary-side resonant components; therefore, the turns ratio, N needs to be considered. They are defined as following equation (20) and (21).

$$L_{r1}{}' = \frac{1}{N^2} L_{r1} \tag{20}$$

$$C_{r1}{}' = N^2 C_{r1} \tag{21}$$

In order to simplify the mathematical expressions of the characteristics gain curves, the definition the parameters are summarized in Table 2.

TABLE 2. Parameter definition for reversed discharging mode.

Parameters	Definition
$m_2 = \frac{L_{r1}{}'}{L_{r2}}$	Resonant inductor ratio
$g_2 = \frac{C_{r1}{}'}{C_{r2}}$	Resonant capacitor ratio
$k_2 = \frac{L_m{}'}{L_{r1}}$	Ratio of magnetizing inductor and resonant inductor
$q_2 = \frac{\sqrt{\frac{L_{r2}}{C_{r2}}}}{R_{eq}{}'}$	Quality factor
$f_{r1\_r} = \frac{1}{2\pi\sqrt{L_{r2}C_{r2}}}$	First resonant frequency
$f_{n1\_r} = \frac{f_s}{f_{r1\_r}}$	The ratio of switching frequency to the first resonant frequency

By substituting the parameters in Table 2 into equation (19), the voltage gain in reversed discharging mode is simplified in equation (22), as shown at the bottom of the next page. This equation shows the relationship between resonant components, quality factor, resonant frequency, and switching frequency.

3) EFFECT OF q (QUALITY FACTOR) VARIATION OF THE GAIN CURVE

As shown in Fig. 13 the influence on the voltage gain is observed by adjusting the value of q_1 when the converter operates in the forward charging mode. The other parameters $k_1 = 3$, $g_1 = 1$, and $m_1 = 1$ are fixed. A high voltage gain can be obtained at the same operating frequency when the design of the q_1 value is low, but the voltage gain curve tends to be flat at the same operating frequency and presents the phenomenon of double-peak voltage gain, thereby increasing the difficulty in the circuit control design when the q_1 value is high. Hence, the q_1 value should avoid being excessively high in the design consideration.

4) EFFECT OF k VALUE VARIATION OF THE GAIN CURVE

As shown in Fig. 14 the influence on the voltage gain is observed by adjusting the value of k_1 when the converter

$$M_{vr\_forward}(f_{n1\_f}) = \frac{1}{\sqrt{\left[1 + \frac{1}{k_1} - \frac{1}{k_1 (f_{n1\_f})^2}\right]^2 + q_1^2 \left[\left(1 + m_1 + \frac{m_1}{k_1}\right) f_{n1\_f} - \frac{\left(1 + \frac{1}{g_1} + \frac{1}{k_1 g_1}\right)}{f_{n1\_f}} + \frac{\left(\frac{1}{k_1 g_1}\right)}{(f_{n1\_f})^3}\right]^2}} \tag{11}$$

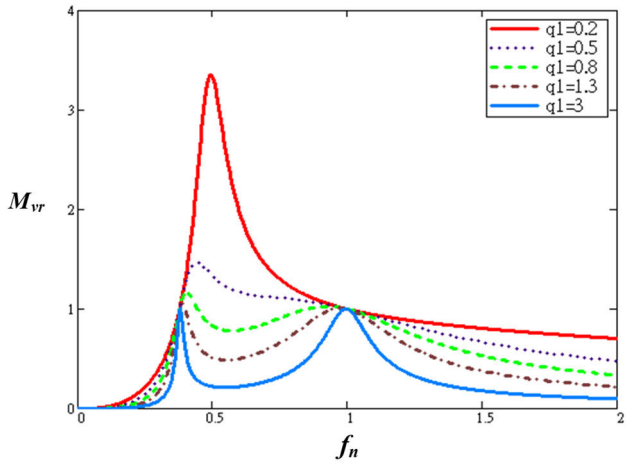

FIGURE 13. Voltage gain curve of different q_1 in forward charging mode.

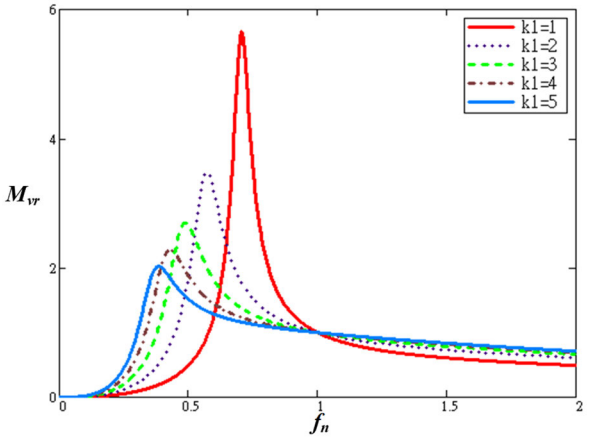

FIGURE 14. Voltage gain curve of different k_1 in forward charging mode.

operates in the forward charging mode. The other parameters $q_1 = 0.25$, $g_1 = 1$, and $m_1 = 1$ are fixed. A high voltage gain can be obtained at the same operating frequency. Besides, the voltage gain for wide voltage output regulation can be achieved when the design of the k_1 value is low. A lower k_1 value corresponds to a low relative magnetizing inductor L_m when the resonant inductor L_r is fixed. Although the coil volume can be reduced, the higher magnetizing current will appear. Thus, the conduction loss will occur in the circuit. Meanwhile, the voltage gain curve is generally flat at the same operating frequency when the value of k_1 is high, and the required frequency adjustment range and magnetizing inductor L_m are high when the output voltage is fixed to ensure that the coil volume increases. Therefore, the design of k_1 value [28], [29] must be considered to meet the voltage gain under the bidirectional wide-range voltage regulation as well as the circuit conversion efficiency and size of the magnetic component, which plays a key role in the circuit design.

5) EFFECT OF g VALUE VARIATION OF THE GAIN CURVE

As shown in Fig. 15 the influence on the voltage gain is observed by adjusting the value of g_1 when the converter operates in the forward charging mode. The other parameters $k_1 = 3$, $q_1 = 0.25$, and $m_1 = 1$ are fixed. A high voltage gain value can be obtained when the design of g_1 value is low, but the two peaks in the voltage gain curve with red color will increase the complexity of designing the voltage regulation. Meanwhile, if the value of g_1 is high, the variation of the voltage gain will be smoother and lower frequency need to be switched to achieve the gain value required for the wide voltage output. Note that a high value denotes a large capacitor volume. Hence, designing an excessively high or low g_1 value is not recommended.

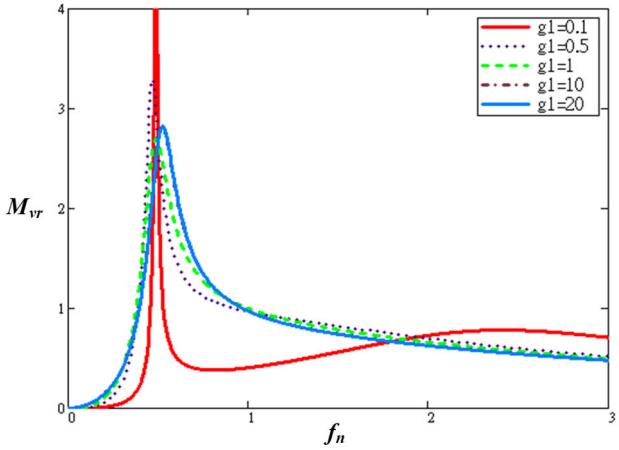

FIGURE 15. Voltage gain curve of different g_1 in forward charging mode.

6) EFFECT OF m VALUE VARIATION OF THE GAIN CURVE

As shown in Fig. 16 the influence of the m_1 value on the voltage gain is observed by modulating m_1 value when the converter operates in the forward charging mode. The other parameters $k_1 = 3$, $q_1 = 0.25$, and $g_1 = 1$ are fixed. On the one hand, the obtained voltage gain curve is flat when m_1 value is low to ensure that a wide frequency range can achieve the voltage gain required for a wide voltage. On the other hand, a high voltage gain can be obtained when m_1 value is high. A high m_1 value corresponds to a high L_{r2} value. A higher resonant inductance indicates a larger circuit volume

$$M_{vr\_reverse}\left(f_{n1\_r}\right) = \frac{1}{\sqrt{\left[1+\frac{1}{k_2}-\frac{1}{k_2(f_{n1\_r})^2}\right]^2 + q_2^2\left[\left(1+m_2+\frac{m_2}{k_2}\right)f_{n1\_D} - \frac{\left(1+\frac{1}{g_2}+\frac{1}{k_2 g_2}\right)}{f_{n1\_r}} + \frac{\left(\frac{1}{k_2 g_2}\right)}{(f_{n1\_r})^3}\right]^2}} \tag{22}$$

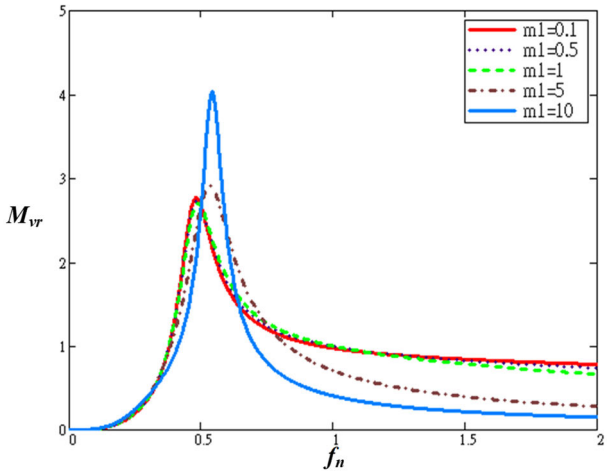

FIGURE 16. Voltage gain curve of different m_1 in forward charging mode.

and loss, thereby reducing the circuit conversion efficiency. Appropriate m value is also a key factor to the performance of efficiency.

III. DESIGN PROCEDURE AND CONSIDERATION

An isolated bidirectional symmetrical resonant converter with a rated output power of 2 kW is established in this study to provide bidirectional energy transfer between the DC grid and battery energy storage ports [30]. According to the lithium battery specifications, the rated working voltage of a battery cell is about 3.6 V, the minimum discharge voltage is 3 V, and the maximum charging voltage is 4.2 V. Hence, the terminal voltage of the battery energy storage and discharge battery [31] in the circuit is 670–800 V. The electrical specifications of the converter are listed in Table 3. In this study, the switching frequency is set for 100kHz according to the following reasons: 1). When the converter is operated at high switching frequency, it allows for the reduction of inductor volume, thereby lowering circuit costs and overall size. 2). High-frequency operation helps reduce the ripple in the output voltage, making it smoother and more stable. 3). Since the proposed converter in this paper adopts the bidirectional LLC resonant circuit structure, it is necessary to consider adjusting the frequency range to control the voltage gain. Choosing 100 kHz as the resonant frequency point allows for a more linear modulation mechanism in the output voltage regulation range.

TABLE 3. Specifications of the proposed converter.

Parameters	Specifications
V_{Grid} (Primary)	400 V
I_{Grid} (Primary)	5 A
V_{Bat} (Secondary)	670~800 V
I_{Bat} (Secondary)	2.5 A
P (Rated power)	2 kW
f_r (Resonant freq.)	100 kHz
f_s (Switching freq.)	75 kHz~130 kHz

A. DESIGN PROCEDURES

The design of resonant parameters of the converter and the selection of components are introduced in this section. The design process is described in detail using a flowchart to understand the circuit design easily. The description of each design process step is shown in Fig. 17 Also, the design steps are discussed as following. (Note: q_1, k_1, g_1, m_1 are parameters for forward charging mode; q_2, k_2, g_2, m_2 are parameters for reverse discharging mode).

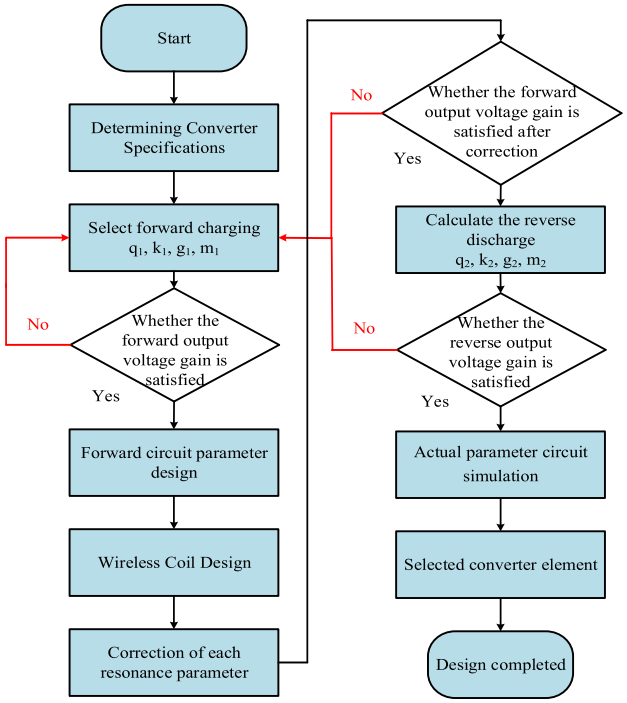

FIGURE 17. Design procedures for resonant parameters.

1) STEP 1. CONSIDER THE CONVERTER SPECIFICATIONS

According to the specifications of this bidirectional converter in Table 3, V_{Grid} (Primary), I_{Grid} (Primary), V_{Bat} (Secondary), and I_{Bat} (Secondary) are the key factors to determine the power level and the turns ratio of the wireless coils. Besides, the resonant components help to achieve soft switching function for all the power switches. The following steps will cover the design process for charging and discharging mode.

2) STEP 2. DETERMINE THE TURNS RATIO OF WIRELESS COILS

The wireless coil turns ratio is first calculated after determining input and output voltage of the converter. The nominal voltage of the battery 800V is selected as the rated output voltage of the battery energy storage port to design the wireless coil as shown in equation (23).

$$N = \frac{N_P}{N_S} = \frac{V_{Grid}}{V_{Bat}} = \frac{400V}{800V} = 0.5 \tag{23}$$

Achieving the soft switching function will be complicated in some output loading levels when the turns ratio is designed from the above formula, and the proposed converter is characterized for a wide output voltage. Therefore, the overall efficiency of the circuit will be influenced. In order to solve this issue, the turns ratio $N = 0.65$ (0.5 multiplies 1.3 times) to ensure the proposed converter with the wireless coils in the bidirectional energy transmission can be operated with soft-switching function.

3) STEP 3. FORWARD CHARGING MODE PARAMETER DESIGN

The wireless coils turns ratio N of the converter is designed to be 0.65, and the maximum and minimum voltage gain values of forward charging mode are calculated as equation (24) and (25).

$$M_{vr\_\max\_for} = \frac{N \cdot V_{Bat\_max}}{V_{Grid\_min}} = \frac{0.65 \cdot 800}{400} \cong 1.31 \quad (24)$$

$$M_{vr\_\min\_for} = \frac{N \cdot V_{Bat\_min}}{V_{Grid\_max}} = \frac{0.65 \cdot 670}{400} = 1.09 \quad (25)$$

Parameter values of q_1, k_1, g_1, and m_1 are then selected to meet the voltage requirements of the forward charging mode. At the same time, the maximum and minimum gain values of the forward charging mode must be considered and the gain curve should be selected. Meanwhile, the curve is designed as the peak singleness to simplify the feedback control. However, the parameters k_1, g_1, and m_1 are fixed and the curve that conforms to each load is selected because q_1 will be affected by the load. The maximum output load power voltage and current of the design standard are 800 V and 2.5 A, respectively. The designed resonant parameters must meet the bidirectional voltage regulation given that this circuit operates in two directions. However, the designed resonant parameters need to be adjusted repeatedly to achieve the bidirectional design requirements because this scheme cannot be accomplished with only one designed parameter. Finally, $q_1 = 0.2$, $k_1 = 3$, $g_1 = 1$, and $m_1 = 1$ are set as the bidirectional voltage gain design of this circuit shown in Fig. 18.

The following equations are used to deduce the parameters of resonant components required for the converter and the wireless coils after determining the values of q_1, k_1, g_1, and m_1:

$$R_{eq} = \frac{8N^2}{\pi^2} \cdot \frac{V_{Bat}}{I_{Bat}} = \frac{8}{\pi^2} \cdot \frac{800}{2.5} \cong 111.8\Omega \quad (26)$$

$$C_{r1} = \frac{1}{2\pi \cdot f_{r1\_f} \cdot R_{eq} \cdot q_1} = \frac{1}{2\pi \cdot 100\text{k} \cdot 111.8 \cdot 0.2} \cong 71nF \quad (27)$$

$$L_{r1} = \frac{1}{(2\pi \cdot f_{r1\_f})^2 \cdot C_{r1}} = \frac{1}{(2\pi \cdot 100\text{k})^2 \cdot 71n} \cong 35.2\mu H \quad (28)$$

$$L_{m1} = L_{r1} \cdot k_1 = 35.2\mu \cdot 3 \cong 105.6\mu H \quad (29)$$

4) STEP 4. REVERSE DISCHARGING MODE PARAMETER DESIGN

The maximum and minimum gain values of the reverse discharge mode can be calculated as equation (30) and (31).

$$M_{vr\_\max\_rev} = \frac{N_r \cdot V_{Grid\_max}}{V_{Bat\_min}} = \frac{1.67 \cdot 400}{670} = 0.997 \quad (30)$$

$$M_{vr\_\min\_rev} = \frac{N_r \cdot V_{Grid\_min}}{V_{Bat\_max}} = \frac{1.67 \cdot 400}{800} = 0.835 \quad (31)$$

where N_r is the turns ratio for reverse discharging mode derived from forward charging mode. Values of q_2, k_2, g_2, and m_2 in the reverse discharging mode are obtained by using equations (32) to (36). Mathcad mathematical analysis software is also applied to determine whether the maximum and minimum gain points of the reverse discharge mode are satisfied, as shown in Fig. 19 If the proposed converter fails to meet the conditions of its voltage gain, then returning to the previous steps is necessary to re-adjust the resonance parameters to meet the voltage gain requirements of the forward charging and reverse discharging modes.

$$R_{eq}{}' = \frac{8}{\pi^2 \cdot N^2} \cdot \frac{V_{Grid}}{I_{Grid}} = \frac{8}{\pi^2 \cdot 1.67^2} \cdot \frac{400}{5} \cong 180.7\Omega \quad (32)$$

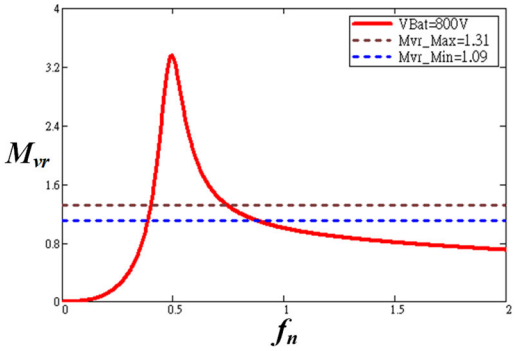

FIGURE 18. Voltage gain curve for operation in forward charging mode.

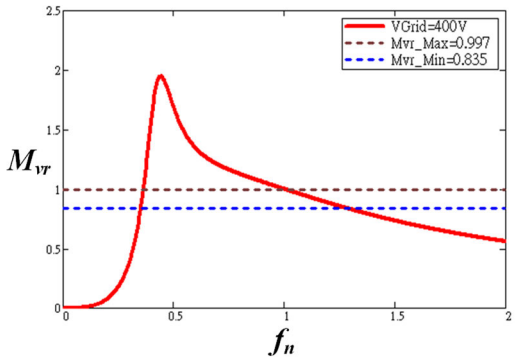

FIGURE 19. Voltage gain curve for operation in reverse discharging mode.

$$k_2 = \frac{\frac{L_{m1}}{N^2}}{L_{r2}} = \frac{\frac{132\mu}{0.65^2}}{102\mu H} \cong 3.3 \tag{33}$$

$$q_2 = \frac{\sqrt{\frac{L_{r2}}{C_{r2}}}}{R_{eq}{}'} = \frac{\sqrt{\frac{102\mu}{24.8n}}}{180.7} \cong 0.35 \tag{34}$$

$$g_2 = \frac{C_{r1}{}'}{C_{r2}} = \frac{N^2 \cdot C_{r1}}{C_{r2}} \cong 0.832 \tag{35}$$

$$m_2 = \frac{L_{r1}{}'}{L_{r2}} = \frac{L_{r1}}{N^2 \cdot L_{r2}} \cong 1.201 \tag{36}$$

5) STEP 5. WIRELESS COILS DESIGN

The winding shape of the wireless coils in this study is circular. In this study, the induction distance is set to 10 mm and the nanocrystalline [32] soft magnetic ferrite pad is selected as the magnetic core to increase the magnetic permeability. The radius of the center inner circle is set to 23 mm because the shape is circular, and the shape of the concentric circle is wound from the innermost circle to the outside. The size of the overall coil disk is about 250 mm×250 mm. The operating frequency of the circuit must be considered and the wire specifications must be designed to improve the skin effect sufficiently. The diameter of the copper is typically less than twice the skin depth to reduce the skin effect. According to the formula circuit's maximum frequency of 130 kHz, the skin depth diameter is about 0.19 mm. Therefore, copper wires with diameters of 0.37 and 0.32 mm are used for the transmitting and receiving coils, and multiple winding methods with Litz wire are utilized to establish the electromagnetic field. The distribution and the current distribution on the wire are uniform.

This study aims to establish a converter for bidirectional transmission that can adjust a wide output voltage for the design of wireless coils. Accordingly, areas of the transmitting(pri.) and receiving(sec.) coils must be as close as possible to the same dimension to facilitate the coupling coefficient of the coil in the forward transmission and the reverse transmission, reach the same coupling coefficient value, and adjust the required voltage. If the difference in the area of the wireless coil is excessively large, then the transmission efficiency will deteriorate. Figs. 20, 21, and 22 show the comparison between the identical and non-identical transmitting/receiving coil area (in Fig.20, rectangular pads with grey color behind the coils are the ferrite pads). The transmission efficiency is higher when the area of the transmitting and receiving coils are almost similar, thereby indicating that the selection of the wire diameter is a key point in wireless coil

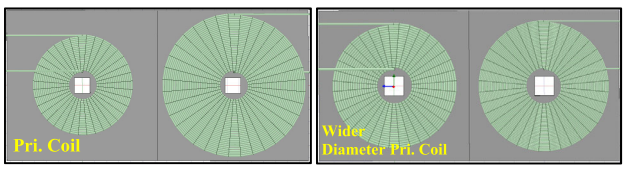

FIGURE 20. Different coil area for Pri. and Sec. (left); identical coil area for Pri. and Sec. (right), (gray rectangular planes are ferrite pads).

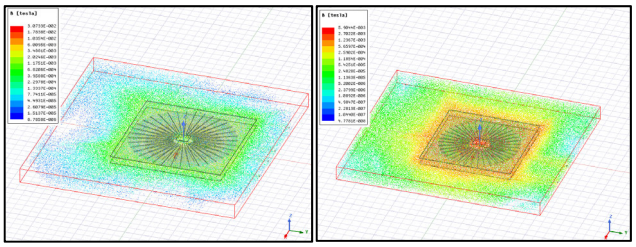

FIGURE 21. Magnetic flux distribution with different coil area for Pri. and Sec. (left); identical coil area for Pri. and Sec. (right).

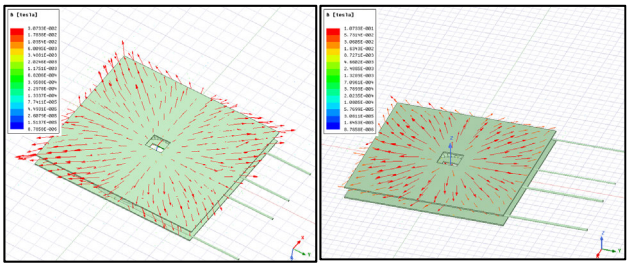

FIGURE 22. The simulation diagram of magnetic line of force with different Pri. and Sec. coil areas (left); identical coil area for Pri. and Sec. (right), (green rectangular planes are ferrite pads).

wound process. The wire diameter on the primary side is about 1.6 times wider than the secondary side to ensure that the area of the wireless coil can reach the same dimension. If the area of the transmitting and receiving coils is different, then the uneven distribution of forward and reverse magnetic lines of force will result in different step-up and down ratios as well as the inability to adjust the output voltage smoothly. According to Fig. 21 the red dot at right is much more than the left which means the magnetic flux distribution is higher. For Fig. 22 the simulation diagram for magnetic line of force at right is much stronger and more concentrated then left. It proves that the coil area for primary and secondary side should be identical to increase the performance of magnetic induction.

B. DIGITAL SIGNAL CONTROLLER APPLICATION

1) CONTROL SYSTEM STRUCTURE

This project uses the digital signal processor TMS320F28335 developed by Texas Instruments as the control core of the double conversion system to carry out bidirectional power regulation and system control strategy planning. Fig. 23 shows the control system architecture of the non-contact resonant converter.

2) FORWARD CHARGING MODE CONTROL SYSTEM

Fig. 24 presents the control system block of the forward charging mode. The battery voltage V_{Bat} passes through the sampling circuit, the sampled value is transmitted to the ADC and then subtracted from the reference voltage signal V_{Bat_ref}, and V_{Bat} goes through the proportional-integral (PI) controller for compensation when the battery is in constant voltage mode. Processing operations are performed

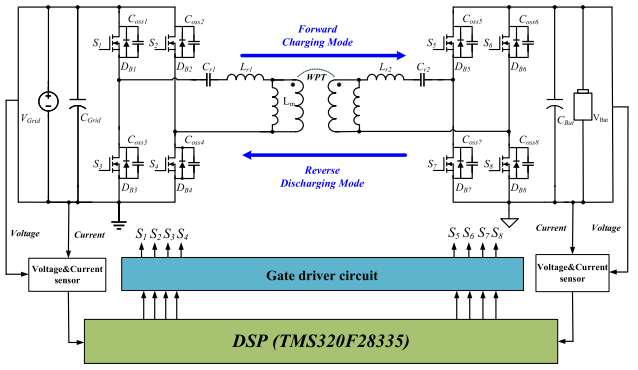

FIGURE 23. Control system architecture of the proposed converter.

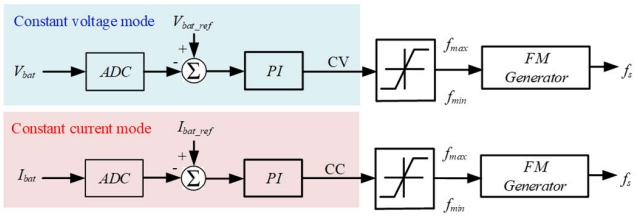

FIGURE 24. Control system block for forward charging mode.

through the frequency generator (FM generator), and a frequency conversion signal PWM is generated and then sent to the main circuit to adjust the power and achieve constant voltage control. In addition, the battery current transmits the sampled value to the ADC through the sampling circuit and then subtracts it from the current reference signal I_{bat_ref} to obtain an error signal value, which is compensated by the proportional-integral (PI) controller and adjusted by the frequency, when the battery enters the current mode. The variable generator performs arithmetic processing to obtain a variable frequency signal PWM. This signal is then sent to the main circuit to adjust the power and achieve constant current control.

3) REVERSE DISCHARGING MODE CONTROL SYSTEM

Fig. 25 shows the control system block of the reverse charging mode. The feedback in this mode will use the constant voltage mode to maintain the stability of the grid voltage. The DC grid voltage V_{grid} passes through the sampling circuit and transmits the sampling value to the ADC. The sampling value is subtracted from the reference voltage signal V_{grid_ref}. The DC grid voltage passes through the proportional integral (PI)controller for compensation via the frequency generator (FM generator) for processing operation to generate a frequency conversion signal PWM. This signal is then sent to the main circuit to adjust the power and achieve constant voltage control.

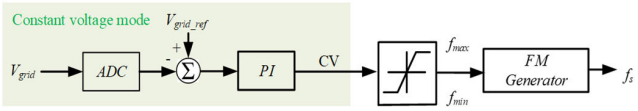

FIGURE 25. Control system block for reverse discharging mode.

IV. EXPERIMENTAL RESULTS

Actual circuit parameters of the converter and the selection of power components are listed in Table 4. The converter is designed according to the circuit parameter and component selection. If the analog circuit is used for control, then the required peripheral circuits are complex, the number of components is large, and the difficulty of circuit design will increase given that the circuit is bidirectionally controlled. Therefore, this study uses the TMS320F28335 digital signal processor developed by Texas Instruments as the system control core of the circuit to realize the bidirectional power regulation between the DC grid and battery ends. This scenario can effectively reduce not only the size of the circuit but also increase its stability and reliability.

TABLE 4. Circuit component parameters and model number.

Parameters	Value / Models
$N_p : N_s$	0.65 : 1
k (Coupling coefficient)	0.957
L_{m1}	132 μH
L_{m2}	340 μH
L_{r1}	44 μH
L_{r2}	102 μH
C_{r1}	57.5 nF
C_{r2}	24.8 nF
DCR of WPT coil for primary	213.5 mΩ (low voltage side)
DCR of WPT coil for secondary	495 mΩ (high voltage side)
S_1~S_8	UJ3C120080KS (1200V/33A)
Digital Signal Controller	TMS320F28335

A. WAVEFORM MEASUREMENT IN FORWARD CHARGING MODE

The experimental waveform of the converter operates in the forward charging mode with full load with an input voltage of $V_{Grid} = 400$ V and output voltage of $V_{Bat} = 800$ V. Fig. 26 presents the measured waveforms of v_{GS3}, v_{DS3}, and i_{DS3}. The waveforms demonstrate that i_{DS3} is in the reverse current state when the power switch S_3 is turned on. This current can release the energy of the parasitic capacitance stored in the power switch to zero. The cross-voltage on the power

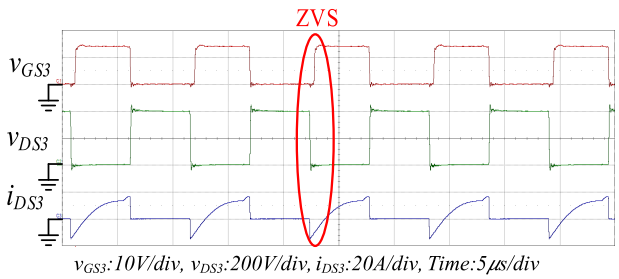

FIGURE 26. Voltage and current waveforms of S3 in forward charging mode.

switch S_3 must be zero and the current should be freewheeling through the intrinsic diode on the power switch to achieve the function of zero-voltage switching.

Fig. 27 shows the experimental waveforms of v_{AB} and i_{Lr1}. The input voltage v_{AB} of the resonant tank is leading of the resonant current i_{Lr1}. At this time, the inductive resonant tank enables the power switch to achieve zero-voltage switching. The transformer will enter the decoupling range and not transfer energy to the secondary side when the resonant current is equal to the magnetizing current and the zero-current switching function can be achieved when the current on the rectifier side drops to zero in advance given that the operating period is greater than the resonant period.

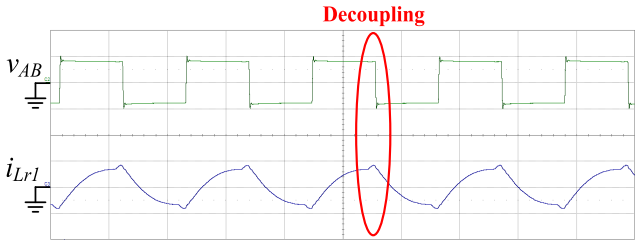

v_{AB}:500V/div, i_{Lr1}:20A/div, Time:5μs/div
(V_{Grid}= 400V, V_{Bat}= 800V, I_{Bat} = 2.5A)

FIGURE 27. v_{AB} and i_{Lr1} waveforms in forward charging mode.

Fig. 28 illustrates the experimental waveforms of v_{DB7} and i_{DB7}. The energy from the primary side is not transmitted to the secondary side and the current of i_{DB7} on the rectifier side drops to zero before the rectifier diode is cut off because the resonant tank enters the decoupling range. Hence, the power switches on the rectifier side can achieve the condition of zero-current switching, and the oscillation on the rectifier diode v_{DB7} in the decoupling interval is caused by the resonance of the parasitic capacitance on the power switch and the resonant inductor on the secondary side.

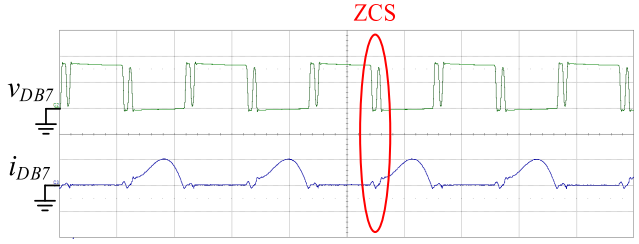

v_{DB7}:500V/div, i_{DB7}:10A/div, Time:5μs/div
(V_{Grid}= 400V, V_{Bat}= 800V, I_{Bat} = 2.5A)

FIGURE 28. v_{DB7} and i_{DB7} waveforms in forward charging mode.

B. WAVEFORM MEASUREMENT IN REVERSE DISCHARGING MODE

The experimental waveform of the converter operates in reverse discharging mode with full load, input voltage of V_{Bat} = 800 V, and output voltage of V_{Grid} = 400 V. Fig. 29 shows the measured waveforms of v_{GS7}, v_{DS7}, and i_{DS7}.

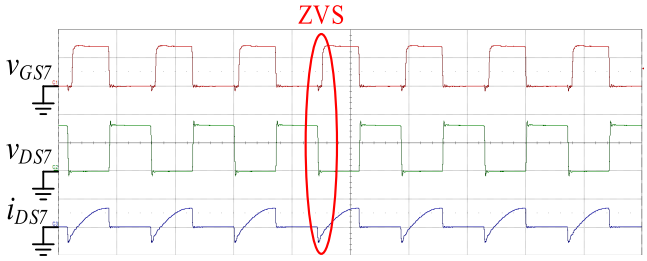

v_{GS7}:10V/div, v_{DS7}:500V/div, i_{DS7}:10A/div, Time:54μs/div
(V_{Bat} = 800V, V_{Grid} = 400V, I_{Grid}= 5A)

FIGURE 29. v_{GS7}, v_{DS7}, i_{DS7} waveforms in reverse discharging mode.

i_{DS7} presents a reverse current state when the power switch S_7 is turned on. This current can release the energy of the parasitic capacitance stored in the power switch to zero. The cross-voltage on the power switch S_7 should be equal to zero and the current must be freewheeling through the intrinsic diode on the power switch to achieve the function of zero-voltage switching.

Fig. 30 shows the measured waveforms of v_{CD} and i_{Lr2}. The input voltage v_{CD} of the resonant tank is leading the resonant current i_{Lr2}. At this time, the inductive resonant tank enables the power switch to achieve zero-voltage switching. The square wave input voltage v_{CD} of the resonant tank of $+V_{Bat}$ and $-V_{Bat}$ is generated by the power switches which are turned on commutatively.

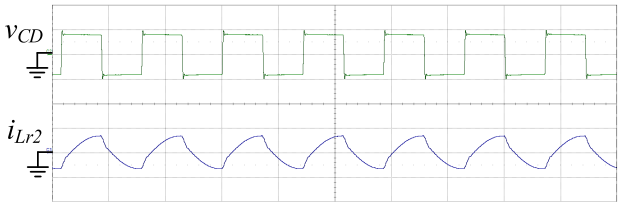

v_{CD}:1kV/div, i_{Lr2}:20A/div, Time:5μs/div
(V_{Bat} = 800V, V_{Grid} = 400V, I_{Grid}= 5A)

FIGURE 30. v_{CD}, i_{Lr2} waveforms in reverse discharging mode.

Fig. 31 depicts the experimental waveforms of v_{DB1} and i_{DB1}. The rectifier diode operating in the first interval before the cut-off neither enters the decoupling interval nor achieves the zero-current switching function.

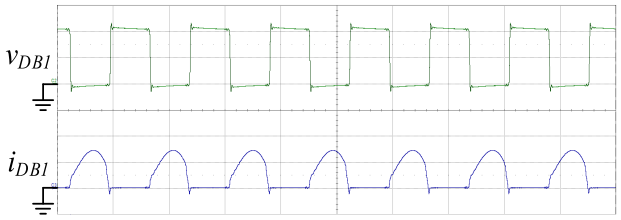

v_{DB1}:200V/div, i_{DB1}:5A/div, Time:5μs/div
(V_{Bat} = 800V, V_{Grid} = 400V, I_{Grid}= 5A)

FIGURE 31. v_{DB1}, i_{DB1} waveforms in reverse discharging mode.

C. DYNAMIC LOAD VARIATION TESTING

Fig. 32 shows the load variation test of the output voltage, where V_{Bat} is the output voltage and I_{Bat} is the output current. The test of changing load current verified whether or not the output voltage can automatically adjust in response to the change of current to achieve the function of stable voltage. Figs. 30(a) and 30(b) presents that the output voltage can realize the function of constant voltage when the load current changes.

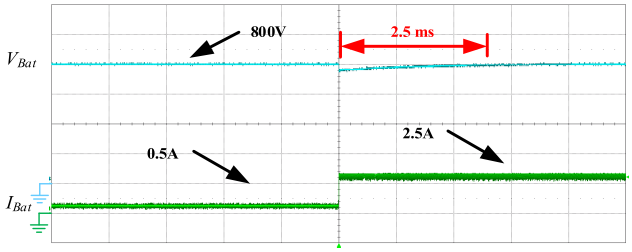

V_{Bat}:200V/div, I_{Bat}:1A/div, Time:1ms/div

(a) V_{Grid}= 400V, V_{Bat}= 800V, I_{Bat}= 0.5A to 2.5A

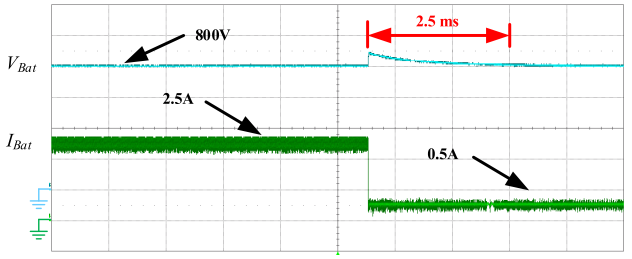

V_{Bat}:200V/div, I_{Bat}:1A/div, Time:1ms/div

(b) V_{Grid}= 400V, V_{Bat}= 800V, I_{Bat}= 2.5A to 0.5A

FIGURE 32. (a), (b) Voltage dynamic load test in forward charging CV mode.

Fig. 33 illustrates the load variation test of the output current, where V_{Bat} is the output voltage and I_{Bat} is the output current. The test of changing load voltage verified whether or not the output current can automatically adjust the output current in response to the voltage change to achieve the function of stable current. Figs. 31(a) and 31(b) depict that the output current It can realize the function of constant current when the load voltage changes.

D. EFFICIENCY ANALYSIS

Fig. 34 shows that the output voltage V_{Bat} is 800 V and the efficiency is measured under different load conditions when the converter works in forward CV mode. The efficiency curve demonstrates that the light-load conversion efficiency is poor and the increase of transmission loss caused by the wireless coil is insignificant with the increase of load because of the influence of the transmission loss of the wireless coil. Therefore, the full-load efficiency improves and the maximum efficiency is 90.2%.

Fig. 35 depicts the converter operated in the forward charging CC mode, an output current I_{Bat} of 2.5 A, and efficiency at different output voltages. Its efficiency is under the condition of a constant current of 2.5 A, the voltage increases when the output voltage is about 780 V, and the maximum efficiency is 90.1%.

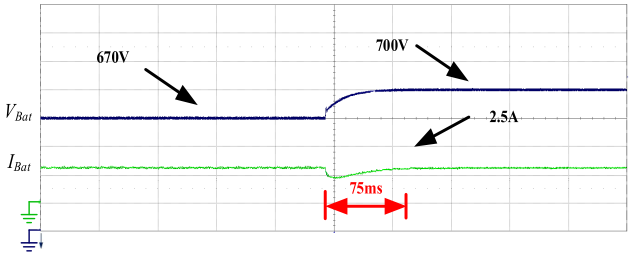

V_{Bat}:20V/div, I_{Bat}:2A/div, Time:50ms/div

(a) V_{Grid}= 400V, I_{Bat}= 2.5A, V_{Bat}= 670V to 700V

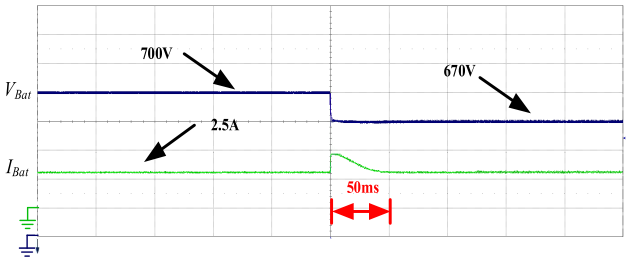

V_{Bat}:20V/div, I_{Bat}:2A/div, Time:50ms/div

(b) V_{Grid}= 400V I_{Bat}= 2.5A V_{Bat}= 700V to 670V

FIGURE 33. (a), (b) Forward charging CC mode current dynamic load test.

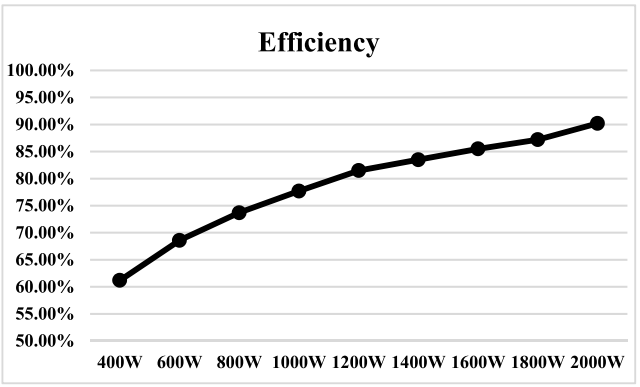

FIGURE 34. Efficiency curve of different load conditions in forward charging CV mode.

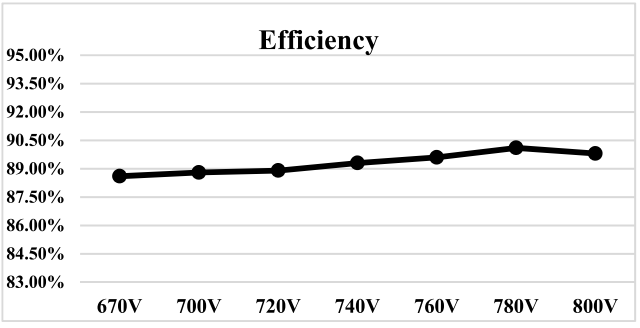

FIGURE 35. Efficiency curve of each load in forward charging CC mode (400V-800V).

Fig. 36 shows the converter operated in reverse discharge mode with an input voltage of V_{Bat} = 670, 740, 800 V; output voltage V_{Grid} of 400 V; and efficiency under different load currents. The maximum efficiency is 91.4%, 89.6%, and 87.8% when the input voltage is 670, 740, and 800 V from the battery side, respectively.

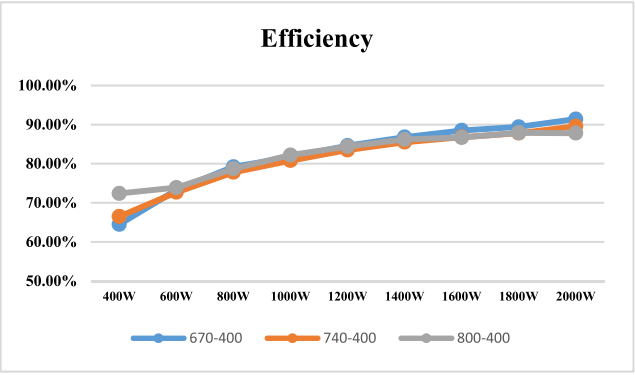

FIGURE 36. Efficiency curves of various loads with different input voltages in reverse discharging mode (800V-400V).

Fig. 37 shows the practical wireless transmitting and receiving coils. Fig. 38 illustrates the complete system.

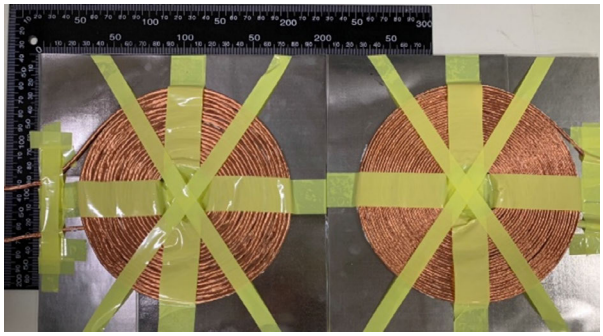

FIGURE 37. Transmitting coil (left) and receiving coil (right). (gray rectangular planes are ferrite pads).

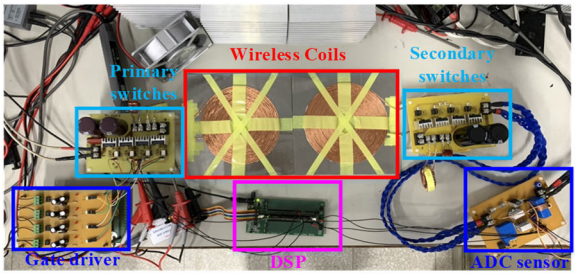

FIGURE 38. The proposed bidirectional wireless charging system.

V. CONCLUSION

A non-contact isolated bidirectional symmetric resonant converter with wide output range is proposed and implemented in this study. The converter improves the traditional LLC resonant converter circuit, adds a resonant element on the secondary side, and replaces the rectifier diode with power switching elements to integrate into a converter that can be used for bidirectional energy transfer to improve the traditional bidirectional energy transfer. The problem of hard switching and small output voltage gain of the converter can improve the overall converter efficiency and realize wide input and output functions. A loosely coupled structure and an inductively coupled wireless energy transmission technology are added to the structure to replace the traditional transformer to a non-contact wireless coil that can transmit energy to the secondary side load terminal by wirelessly. Moreover, the converter presents the functions of constant voltage (CV) and constant current (CC) charging modes which are suitable for EV charging system in the future. The proposed research focuses on the application of bidirectional wireless charging between a low-voltage side with DC grid of 400V and a high-voltage side with 800V electric vehicle battery. This contribution significantly enhances the versatility of wireless charging applications.

REFERENCES

[1] A. S. Babokany, M. Jabbari, G. Shahgholian, and M. Mahdavian, "A review of bidirectional dual active bridge converter," in *Proc. 9th Int. Conf. Electr. Eng./Electron., Comput., Telecommun. Inf. Technol.*, May 2012, pp. 1–4.

[2] K. Tytelmaier, O. Husev, O. Veligorskyi, and R. Yershov, "A review of non-isolated bidirectional DC–DC converters for energy storage systems," in *Proc. 2nd Int. Young Scientist Forum Appl. Phys. Eng. (YSF)*, Oct. 2016, pp. 22–28.

[3] L. Qu, X. Wang, D. Zhang, Z. Bai, and Y. Liu, "A high efficiency and low shutdown current bidirectional DC–DC CLLLC resonant converter," in *Proc. 22nd Int. Conf. Electr. Mach. Syst. (ICEMS)*, Aug. 2019, pp. 1–6, doi: 10.1109/ICEMS.2019.8922079.

[4] R. Zgheib, K. Al-Haddad, and I. Kamwa, "V2G, G2V and active filter operation of a bidirectional battery charger for electric vehicles," in *Proc. IEEE Int. Conf. Ind. Technol. (ICIT)*, Mar. 2016, pp. 1260–1265, doi: 10.1109/ICIT.2016.7474935.

[5] Z. U. Zahid, Z. M. Dalala, R. Chen, B. Chen, and J.-S. Lai, "Design of bidirectional DC–DC resonant converter for vehicle-to-grid (V2G) applications," *IEEE Trans. Transport. Electrific.*, vol. 1, no. 3, pp. 232–244, Oct. 2015, doi: 10.1109/TTE.2015.2476035.

[6] Y. Zhou and C. Ngai-Man Ho, "A review on microgrid architectures and control methods," in *Proc. IEEE 8th Int. Power Electron. Motion Control Conf.*, May 2016, pp. 3149–3156.

[7] W. Zhang and J. Wang, "Research on V2G control of smart microgrid," in *Proc. Int. Conf. Comput. Eng. Intell. Control (ICCEIC)*, Nov. 2020, pp. 216–219.

[8] R. G. Gago, S. F. Pinto, and J. F. Silva, "G2V and V2G electric vehicle charger for smart grids," in *Proc. IEEE Int. Smart Cities Conf. (ISC2)*, Sep. 2016, pp. 1–6, doi: 10.1109/isc2.2016.7580786.

[9] B. Zhao, X. Zhang, and J. Huang, "AI algorithm-based two-stage optimal design methodology of high-efficiency CLLC resonant converters for the hybrid AC–DC microgrid applications," *IEEE Trans. Ind. Electron.*, vol. 66, no. 12, pp. 9756–9767, Dec. 2019.

[10] I. Aghabali, J. Bauman, P. J. Kollmeyer, Y. Wang, B. Bilgin, and A. Emadi, "800-V electric vehicle powertrains: Review and analysis of benefits, challenges, and future trends," *IEEE Trans. Transport. Electrific.*, vol. 7, no. 3, pp. 927–948, Sep. 2021.

[11] J.-W. Kim, M.-H. Park, B.-H. Lee, and J.-S. Lai, "Analysis and design of LLC converter considering output voltage regulation under no-load condition," *IEEE Trans. Power Electron.*, vol. 35, no. 1, pp. 522–534, Jan. 2020.

[12] R.-L. Lin and C.-W. Lin, "Design criteria for resonant tank of LLC DC–DC resonant converter," in *Proc. IECON - 36th Annu. Conf. IEEE Ind. Electron. Soc.*, Nov. 2010, pp. 427–432.

[13] R.-L. Lin and L.-H. Huang, "Efficiency improvement on LLC resonant converter using integrated LCLC resonant transformer," in *Proc. IEEE Ind. Appl. Soc. Annu. Meeting*, Oct. 2016, pp. 1–8, doi: 10.1109/IAS.2016.7731862.
[14] T. Krigar and M. Pfost, "2-MHz compact wireless power transfer system with voltage conversion from 400 V to 48 V," in *Proc. IEEE Wireless Power Transf. Conf. (WPTC)*, Jun. 2021, pp. 1–4, doi: 10.1109/WPTC51349.2021.9457887.
[15] Y. Liu, U. K. Madawala, R. Mai, and Z. He, "Zero-Phase-Angle controlled bidirectional wireless EV charging systems for large coil misalignments," *IEEE Trans. Power Electron.*, vol. 35, no. 5, pp. 5343–5353, May 2020.
[16] F. Liu, K. Li, K. Chen, and Z. Zhao, "A phase synchronization technique based on perturbation and observation for bidirectional wireless power transfer system," *IEEE J. Emerg. Sel. Topics Power Electron.*, vol. 8, no. 2, pp. 1287–1297, Jun. 2020.
[17] R. Tavakoli and Z. Pantic, "Analysis, design, and demonstration of a 25-kW dynamic wireless charging system for roadway electric vehicles," *IEEE J. Emerg. Sel. Topics Power Electron.*, vol. 6, no. 3, pp. 1378–1393, Sep. 2018.
[18] X. Dai, J.-C. Jiang, and J.-Q. Wu, "Charging area determining and power enhancement method for multiexcitation unit configuration of wirelessly dynamic charging EV system," in *Proc. IEEE Trans. Ind. Electron.*, May 2019, vol. 66, no. 5, pp. 4086–4096.
[19] F. Lin, X. Zhang, and X. Li, "Design methodology for symmetric CLLC resonant DC transformer considering voltage conversion ratio, system stability, and efficiency," *IEEE Trans. Power Electron.*, vol. 36, no. 9, pp. 10157–10170, Sep. 2021.
[20] J. Huang and X. Zhang, "Three-step switching frequency selection criteria for symmetrical CLLC-type DC transformer in hybrid AC/DC microgrid," *IEEE Trans. Power Electron.*, vol. 34, no. 10, pp. 9379–9385, Oct. 2019.
[21] S. Senthilkumar, M. Haidari, G. Devi, A. S. F. Britto, R. Gorthi, and M. Sivaramkrishnan, "Wireless bidirectional power transfer for E-vehicle charging system," in *Proc. Int. Conf. Edge Comput. Appl. (ICECAA)*, Tamilnadu, India, Oct. 2022, pp. 705–710, doi: 10.1109/ICECAA55415.2022.9936175.
[22] J. Huang, X. He, P. Huo, and R. Xu, "A hybrid modulation strategy for LCC–LCC compensated bidirectional wireless power transfer system to achieve high efficiency in the whole operating range," *IEEE Trans. Ind. Electron.*, pp. 1–10, Jan. 2023, doi: 10.1109/TIE.2023.3247774.
[23] M. Mohammad, O. C. Onar, G.-J. Su, J. Pries, V. P. Galigekere, S. Anwar, E. Asa, J. Wilkins, R. Wiles, C. P. White, and L. E. Seiber, "Bidirectional LCC–LCC-compensated 20-kW wireless power transfer system for medium-duty vehicle charging," *IEEE Trans. Transport. Electrific.*, vol. 7, no. 3, pp. 1205–1218, Sep. 2021, doi: 10.1109/TTE.2021.3049138.
[24] J. Zheng, S. Lu, and J. Li, "LLC and LCC analysis and comparison of resonant converters," in *Proc. 35th Youth Academic Annu. Conf. Chin. Assoc. Autom. (YAC)*, Oct. 2020, pp. 226–231.
[25] H. -T. Chang, T. -J. Liang, and W. -C. Yang, "Design and implementation of bidirectional DC–DC CLLLC resonant converter," in *Proc. IEEE Energy Convers. Congr. Expo. (ECCE)*, Jun. 2018, pp. 2712–2719, doi: 10.1109/ECCE.2018.8557697.
[26] W. Han, R. Mal, and L. Corradini, "Analysis and design methodology for ZVS phase shift modulated bidirectional CLLLC resonant DC–DC converters," in *Proc. 21st Eur. Conf. Power Electron. Appl.*, Sep. 2019, pp. P.1–P.10, doi: 10.23919/EPE.2019.8914864.
[27] V.-B. Vu, V.-T. Phan, M. Dahidah, and V. Pickert, "Multiple output inductive charger for electric vehicles," *IEEE Trans. Power Electron.*, vol. 34, no. 8, pp. 7350–7368, Aug. 2019.
[28] S.-T. Wu and C.-H. Han, "Design and implementation of a full-bridge LLC converter with wireless power transfer for dual mode output load," *IEEE Access*, vol. 9, pp. 120392–120406, 2021.
[29] P. Jia, T. Guo, X. Zhu, and T. Shao, "A control strategy for the bidirectional LLC-L converter to extend the gain range based on the time domain analytical model," *IEEE Trans. Power Electron.*, vol. 38, no. 4, pp. 4876–4893, Apr. 2023.
[30] J.-Y. Lee and B.-M. Han, "A bidirectional wireless power transfer EV charger using self-resonant PWM," *IEEE Trans. Power Electron.*, vol. 30, no. 4, pp. 1784–1787, Apr. 2015.
[31] S. Y. Chu, X. Cui, X. Zan, and A.-T. Avestruz, "Transfer-power measurement using a non-contact method for fair and accurate metering of wireless power transfer in electric vehicles," *IEEE Trans. Power Electron.*, vol. 37, no. 2, pp. 1244–1271, Feb. 2022.
[32] M. Xiong, X. Wei, Y. Huang, Z. Luo, and H. Dai, "Research on novel flexible high-saturation nanocrystalline cores for wireless charging systems of electric vehicles," *IEEE Trans. Ind. Electron.*, vol. 68, no. 9, pp. 8310–8320, Sep. 2021.

SEN-TUNG WU was born in Taipei, Taiwan, in 1980. He received the B.S., M.S., and Ph.D. degrees from the Department of Electronic and Computer Engineering, National Taiwan University of Science and Technology, Taiwan, in 2003, 2005, and 2014, respectively. He had working experience with the Research and Development Department of switching power supply design manufacture for several years. In 2017, he was an Assistant Professor with the Department of Electrical Engineering, National Formosa University, Yunlin, Taiwan. He has been an Associate Professor with the EE Department, since 2022. His main research interests include power electronics, energy converter designs, battery chargers, bidirectional converters, power factor correction circuit design, and wireless power transfer applications.

YU-WEI CHIU is from Chaiyi City, Taiwan. He received the B.S. and M.S. degrees from the Department of Electrical Engineering, National Formosa University, in 2020 and 2022, respectively. He has been with LITE-ON Technology Company, Taiwan, as an EE Research and Development Engineer, since 2023. He is currently in charge of a DC/DC wireless EV charger circuit design project for high power. His research interests include power electronics, wireless power transfer applications, bidirectional converter design, and circuit analysis.